

CrossMark
click for updatesCite this: *J. Mater. Chem. A*, 2014, 2, 20288

A simultaneous increase in the ZT and the corresponding critical temperature of p-type $\text{Bi}_{0.4}\text{Sb}_{1.6}\text{Te}_3$ by a combined strategy of dual nanoinclusions and carrier engineering†

Ye Xiao,^a Jun-you Yang,^{*a} Qing-hui Jiang,^a Liang-wei Fu,^a Yu-bo Luo,^a Ming Liu,^a Dan Zhang,^a Ming-yang Zhang,^a Wei-xin Li,^a Jiang-ying Peng^b and Fu-qiang Chen^c

By means of $\beta\text{-Zn}_4\text{Sb}_3$ addition and thermal decomposition, dual nanoinclusions of Zn and ZnSb were introduced and Zn atoms were doped into p-type $\text{Bi}_{0.4}\text{Sb}_{1.6}\text{Te}_3$ successfully. Due to the increase of hole concentration by Zn doping and band structure optimization, the bipolar conduction was suppressed and the intrinsic excitation shifts to higher temperature. The power factors of the samples were slightly improved, while the lattice thermal conductivities of the samples were greatly reduced due to the extra phonon scattering introduced by the dual nanoinclusions. As a result, the critical temperature corresponding to the maximum ZT value was greatly increased to 423 K, which is about 120 K higher when compared with the conventional Bi_2Te_3 -based materials. A maximum ZT of 1.44 was achieved for the sample with 1.5 wt% $\beta\text{-Zn}_4\text{Sb}_3$ at 423 K, which is also the highest ZT value ever reported at such a high temperature for p-type Bi_2Te_3 -based materials. This work is of importance to expand the application of Bi_2Te_3 -based materials for low grade waste-heat recovery.

Received 2nd September 2014
Accepted 1st October 2014

DOI: 10.1039/c4ta04558k

www.rsc.org/MaterialsA

Introduction

Solid-state energy conversion between heat and electricity power by thermoelectric materials in the fields of waste-heat recovery and refrigeration has gained enormous interest during the last few decades.¹ The conversion efficiency is governed by the figure of merit ($ZT = \alpha^2 T / \rho \kappa$) of a thermoelectric material, where α is the Seebeck coefficient, ρ is the electrical resistivity, κ is the thermal conductivity and T is the absolute temperature. The ZT value remains about unity for decades because of the high interdependence of those parameters, and how to improve the ZT value and increase the energy conversion efficiency is certainly the ultimate pursuit of researchers on thermoelectric materials. By now, many compounds have been studied for potential thermoelectric applications, such as Bi_2Te_3 -based, PbTe -based, CoSb_3 -based and Si-Ge based materials, for different temperature regions.^{2–4} Among them, Bi_2Te_3 -based materials are the most competitive candidates for low grade

waste-heat recovery and thermoelectric cooling around room temperature. Bismuth telluride crystallizes in a rhombohedral lattice which consists of a sequential layer of $\text{Te}(1)\text{-Bi-Te}(2)\text{-Bi-Te}(1)$ along the c axis, and presents an anisotropic thermoelectric performance. Currently, most of the Bi_2Te_3 -based materials available for mass production are still single crystals or unidirectional polycrystals, which are usually grown by zone melting based technologies, such as Bridgman⁵ and Czochralski methods,⁶ etc. With years of studies, the doping strategy and crystal growth techniques for Bi_2Te_3 -based single crystals or unidirectional polycrystalline materials have continued to mature. However, single crystalline or unidirectional polycrystalline Bi_2Te_3 -based materials are apt to cleave along the basal plane due to the weak van der Waals bonding between the $\text{Te}(1)\text{-Te}(1)$ layers thus degrading their machinability for thermoelectric modules. Therefore, polycrystalline Bi_2Te_3 -based materials with a randomly orientated microstructure and high thermoelectric performance are more preferable for practical applications, and more and more attention has been paid to polycrystalline materials since the 1980s. In general, the efforts to improve the ZT value of polycrystalline Bi_2Te_3 -based materials are mainly focused on the fabrication process optimization to modify the microstructure of the rhombohedral compounds. Up to now, different techniques, such as BMA-HP,⁷ MA-HP,⁸ MA-ECAE,⁹ MS-SPS,¹⁰ and hot-forging,¹¹ have been employed to fabricate polycrystalline materials and improve their thermoelectric properties, and

^aState Key Laboratory of Material Processing and Die & Mould Technology, Huazhong University of Science and Technology, Wuhan 430074, P. R. China. E-mail: jyyang@mail.hust.edu.cn

^bSchool of Mechanical Science and Engineering, Huazhong University of Science & Technology, Wuhan 430074, P. R. China

^cState Key Laboratory of Laser Propulsion & Application, Equipment Academy, Beijing 101400, P. R. China

† Electronic supplementary information (ESI) available: Estimation of relaxation time and other information. See DOI: 10.1039/c4ta04558k

encouraging results have been obtained successively.^{12,13} It is noteworthy that the effective working temperature range for both single crystal and polycrystalline Bi_2Te_3 -based materials, which corresponds to the optimal ZT value, is mostly in the region of 298–350 K, and the ZT value declines rapidly once the temperature rises beyond the region due to the intrinsic excitations. However, from the related statistics,¹⁴ most of the low grade industrial waste heat is in the region of 350–473 K, which is quite an awkward range because it is just beyond the optimal working region for the present Bi_2Te_3 -based materials while other thermoelectric materials, such as PbTe and filled skutterudites, do not reach their appropriate working conditions. Therefore it will be of great significance to the low grade waste-heat recovery to shift the optimal temperature corresponding to the maximum ZT value of Bi_2Te_3 -based materials into the related region. Generally, the increase of intrinsic excitation temperature indicates the widening of the energy gap. That is to say, to raise the optimal temperature of Bi_2Te_3 -based materials, their band structure should be optimized; therefore their composition must be regulated appropriately.

As mentioned above, the composition system of Bi_2Te_3 -based materials has already matured. It is very challenging to adjust the composition and band structure without obvious degradation of their thermoelectric performance by conventional doping or alloying methods. Therefore a new strategy should be adopted to optimize the band structure and raise the optimal temperature of Bi_2Te_3 -based materials. In this work, $\beta\text{-Zn}_4\text{Sb}_3$ was added to the p-type $\text{Bi}_{0.4}\text{Sb}_{1.6}\text{Te}_3$ matrix, by means of the decomposition of $\beta\text{-Zn}_4\text{Sb}_3$ into Zn and ZnSb nanoparticles,¹⁵ the bipolar conduction of $\text{Bi}_{0.4}\text{Sb}_{1.6}\text{Te}_3$ was inhibited and shifted to higher temperature due to the band structure optimization. Furthermore, the phonon thermal conductivity was greatly reduced by the ZnSb and Zn nanoinclusions. As a result, the optimal working temperature corresponding to the maximum ZT value increases by about 100 K to 423 K when compared to the present Bi_2Te_3 -based single crystalline and polycrystalline materials, and a maximum ZT of 1.44 has been achieved at 423 K in the sample with the addition of 1.5 wt% $\beta\text{-Zn}_4\text{Sb}_3$, which is also the highest ZT value that has ever been reported at such a high temperature for p-type Bi_2Te_3 -based materials.

Experimental

Elemental powder mixtures of Bi (200 mesh, 99.99 wt%), Sb (200 mesh, 99.99 wt%), and Te (200 mesh, 99.99 wt%) were weighed according to the composition of $\text{Bi}_{0.4}\text{Sb}_{1.6}\text{Te}_3$ and loaded into a stainless-steel vial with a ball-to-powder ratio of 20 : 1 for mechanical alloying (MA), and the MA process was conducted in a planetary ball mill at a speed of 400 rpm for 12 h under the protection of a purified argon atmosphere. The $\beta\text{-Zn}_4\text{Sb}_3$ compound ingot was synthesized as follows: the precursor of the elemental Zn shot (99.99 wt%) and Sb shot (99.99 wt%) mixture was sealed in an evacuated quartz tube and melted at 1023 K for 24 hours and then quenched in cool water for the $\beta\text{-Zn}_4\text{Sb}_3$ single phase compound. Subsequently, the $\beta\text{-Zn}_4\text{Sb}_3$ ingot was crushed manually and then ball milled at 400 rpm for

5 h to obtain fine powders. After that, different contents of $\beta\text{-Zn}_4\text{Sb}_3$ powders were added to the as-MAed $\text{Bi}_{0.4}\text{Sb}_{1.6}\text{Te}_3$ powders and further mixed by ball milling at 300 rpm for 2 h. Finally, the powder mixtures with different contents of $\beta\text{-Zn}_4\text{Sb}_3$ were consolidated by hot press at 753 K under a pressure of 100 MPa for 2 h in a purified argon atmosphere. The relative density is above 95% for all the hot pressed samples.

The structure and phase purity of the samples were analyzed by X-ray diffraction (XRD) (Philip X'Pert PRO, with Cu K α radiation, $\lambda = 0.15418$ nm). The fractographs and microstructures of the samples were observed with a field-emission scanning electron microscope (FESEM) (NanoSEM 450), and high resolution transmission electron microscopy (HRTEM) observation and energy dispersive X-ray spectroscopy (EDS) microanalysis were performed with a JEM-2100F transmission electron microscope working in bright-field mode at an accelerating voltage of 200 kV. Seebeck coefficient and electrical resistivity were simultaneously measured with a Namicro-III Thermoelectric measurement system.¹⁶ Thermal conductivity is calculated in the light of $\kappa = DC_p\lambda$, where the density (D) was determined by the Archimedes method, the specific heat capacity (C_p) was derived by using a differential scanning calorimeter (PerkinElmer Diamond DSC) and the thermal diffusivity λ was measured using the laser flash diffusivity method with a LFA-427 (NETZSCH) machine. The heat flow is in the same direction as the electrical current during measurements to eliminate the inappropriate calculation of the figure of merit in the case of orientation existing in samples. The Hall measurements were accomplished by the Van der Pauw method in a Hall measurement system (HMS-5500).

Results and discussion

Fig. 1(a) shows the X-ray diffraction (XRD) patterns of polycrystalline $\text{Bi}_{0.4}\text{Sb}_{1.6}\text{Te}_3$ with different contents of $\beta\text{-Zn}_4\text{Sb}_3$ ($x = 0\text{--}2.5$ wt%).

It can be seen that all the diffraction peaks can be indexed to the rhombohedral $\text{Bi}_{0.4}\text{Sb}_{1.6}\text{Te}_3$ based on the ICSD card (PDF# 01-072-1836). The magnified diffraction peaks shown in Fig. 1(b) shift to a high angle direction with increasing the amount of $\beta\text{-Zn}_4\text{Sb}_3$ up to 1.5 wt%, and no shift can be observed on further increasing the amount of $\beta\text{-Zn}_4\text{Sb}_3$. It indicates that the lattice of $\text{Bi}_{0.4}\text{Sb}_{1.6}\text{Te}_3$ solid solution shrinks with an increase of $\beta\text{-Zn}_4\text{Sb}_3$, and it gets saturated when the content of $\beta\text{-Zn}_4\text{Sb}_3$ is over 1.5 wt%. The shrinkage of the lattice means that some heteroatoms from $\beta\text{-Zn}_4\text{Sb}_3$ dissolved into the lattice of $\text{Bi}_{0.4}\text{Sb}_{1.6}\text{Te}_3$. However, $\beta\text{-Zn}_4\text{Sb}_3$ as a compound is unable to dope into the lattice, the only possibility is Zn or Sb doping which may come from the $\beta\text{-Zn}_4\text{Sb}_3$. It is reported that $\beta\text{-Zn}_4\text{Sb}_3$ decomposed into Zn and ZnSb at about 673 K.¹⁵ Thus the lattice shrinkage of $\text{Bi}_{0.4}\text{Sb}_{1.6}\text{Te}_3$ should be caused by the doping of Zn from the decomposed $\beta\text{-Zn}_4\text{Sb}_3$, and the TEM observation shown later also presents the ZnSb and Zn nanoinclusions and confirms the decomposition of $\beta\text{-Zn}_4\text{Sb}_3$. There are three possible sites for Zn doping in the $\text{Bi}_{0.4}\text{Sb}_{1.6}\text{Te}_3$ lattice: the substitution site on Bi/Sb, the intercalation site between two van der Waals bonding layers of Te(1)–Te(1) and the substitution on

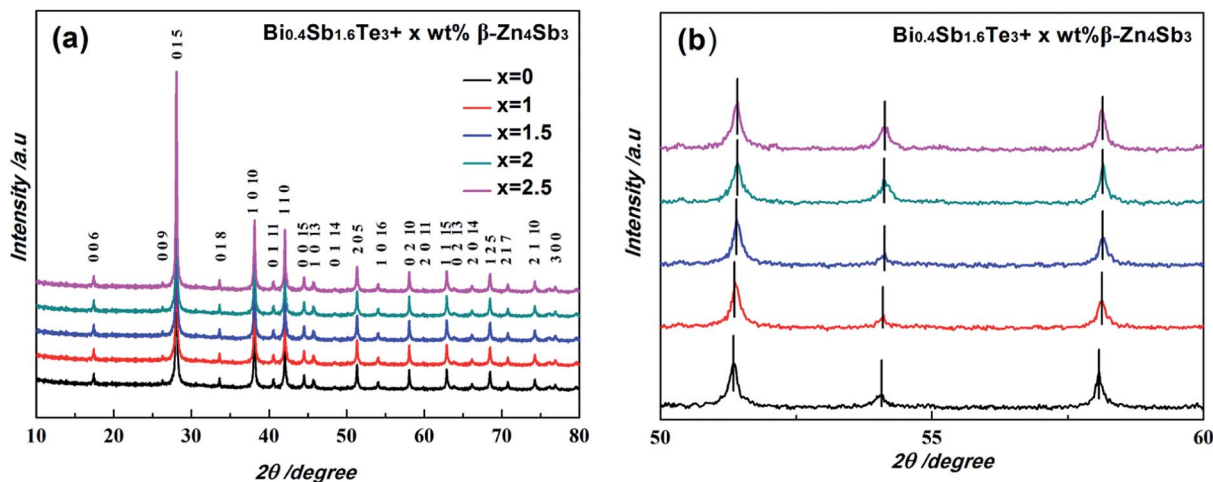
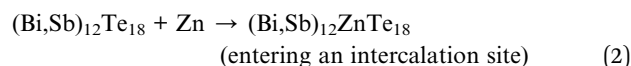
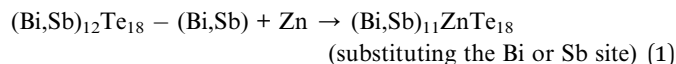


Fig. 1 (a) XRD patterns of the samples with $\text{Bi}_{0.4}\text{Sb}_{1.6}\text{Te}_3 + x \text{ wt}\% \beta\text{-Zn}_4\text{Sb}_3$ and (b) high angle XRD peak position comparison of the samples.

the Te site. Apparently, the possibility for Zn doping on the Te site as the anion is quite low because Zn tends to contribute its valence electrons. As known, the radius of Zn^{2+} is 74 pm, Bi^{3+} is 108 pm and Sb^{3+} is 92 pm. From the view of the ion radius, the lattice would expand if Zn entered into a position between two van der Waals bonding layers of $\text{Te}(1)\text{-Te}(1)$, and if Zn substitutes the Bi/Sb site, the lattice will shrink because the radius of Zn^{2+} is smaller than that of Bi^{3+} or Sb^{3+} , and the excess Bi or Sb will form anti-site defects.¹⁷

In order to confirm the assumption, a calculation of formation energy was carried out (see details in ESI. 1†) to determine the most preferential site for Zn atoms to occupy and is shown as follows:¹⁸



Therefore

$$E_f = E_t\{(\text{Bi,Sb})_{11}\text{ZnTe}_{18}\} - E_t\{(\text{Bi,Sb})_{12}\text{Te}_{18}\} - E_t\{\text{Zn}\} + E_t\{(\text{Bi,Sb})_1\} \quad (3)$$

$$E_f = E_t\{(\text{Bi,Sb})_{12}\text{ZnTe}_{18}\} - E_t\{(\text{Bi,Sb})_{12}\text{Te}_{18}\} - E_t\{(\text{Bi,Sb})_1\} \quad (4)$$

where E_f is the formation energy and E_t is the total energy of each material.

Density of states (DOS) (Fig. 2) calculation predicts an n-type transport behavior for Zn in the intercalation site while a p-type behavior in the substitution site for Bi or Sb atoms. The carrier concentration shown in Table 1 also confirms that Zn substitutes for the Bi or Sb site because the hole concentration increases with the content of $\beta\text{-Zn}_4\text{Sb}_3$, which is in good consistence with the above results of DOS calculation and XRD analysis.

Fig. 3 shows the SEM fractographs of the samples with different contents of $\beta\text{-Zn}_4\text{Sb}_3$ ($x = 0, 1.0$, and 1.5), the EDS results of other samples are also given in ESI. 2 (Fig. S1†). It can be seen that the samples are polycrystalline with randomly oriented grains. In comparison with the $\beta\text{-Zn}_4\text{Sb}_3$ free sample (Fig. 3(a)), some nanoscale white particles appear in the 1.0 wt% sample in Fig. 3(b), and the nano-inclusions are distributed

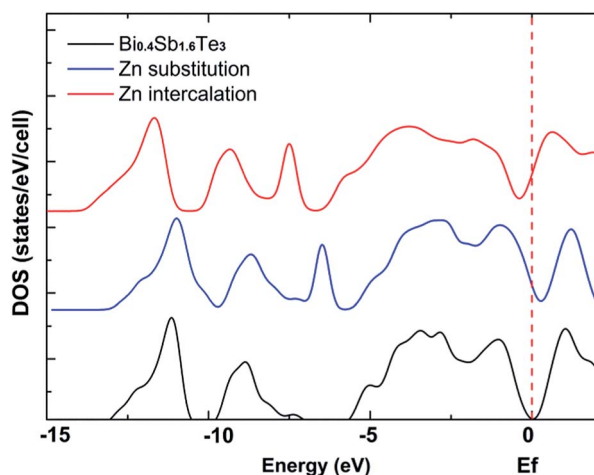


Fig. 2 The calculated DOS for $\text{Bi}_{0.4}\text{Sb}_{1.6}\text{Te}_3$ and the Zn doped $\text{Bi}_{0.4}\text{Sb}_{1.6}\text{Te}_3$, where the Fermi level has been specified to zero. After doping, the Fermi level moves into the valence band when Zn substitutes the Bi or Sb site while the conduction band for Zn enters an intercalation site, respectively.

Table 1 Carrier concentration n_h , Hall mobility μ_H of all the samples at room temperature

Composition ($x \text{ wt}\%$)	n_h (10^{19} cm^{-3})	μ_H ($\text{cm}^2 \text{ V}^{-1} \text{ s}^{-1}$)
0	2.7	192
1.0	3.5	185
1.5	4.0	156
2.0	4.3	138
2.5	4.4	126

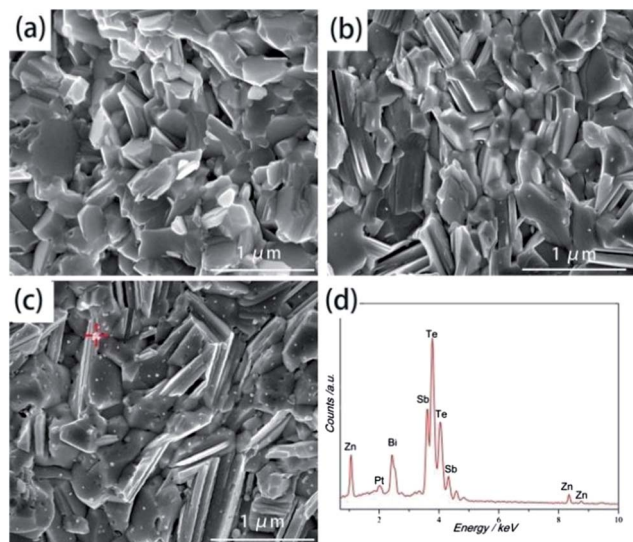


Fig. 3 FESEM fractographs of the samples with the content of β -Zn₄Sb₃ $x = 0$ (a), $x = 1$ (b) and $x = 1.5$ (c), respectively. (d) EDS composition analysis of the nano-inclusion marked in (c).

homogeneously and their amount increases when the content of β -Zn₄Sb₃ increases to 1.5% (Fig. 3(c)). The EDAX results in Fig. 3(d) indicate that the nano-inclusions are Zn-containing particles resulting from β -Zn₄Sb₃.

To further understand the nature of the nano-inclusions, a high resolution transmission electron microscope (HRTEM) was employed to characterize the structure and composition of the nano-inclusions. As shown in Fig. 4(a), the grains have a polygonal morphology and some nano-inclusions can be found in the field of view.

Two nanoparticles, marked with circles 1 and 2 in Fig. 4(a), were further magnified and analyzed. The inter-planar spacing of 1.64 Å in zone 1 shown in Fig. 4(b) is in good agreement with that of the Zn (102) plane, indicating that the nanoparticle in zone 1 is a Zn nanoparticle (see the corresponding EDAX results in ESI. 3, Fig. S2†). Fig. 4(c) shows the magnified image of the nano-inclusion located at the triple-junction grain boundary in zone 2, and the planes with a spacing of 3.14 Å (Fig. 4(d)) accord very well with the (112) plane of the ZnSb compound and the fast Fourier transformation pattern represented in the inset of Fig. 4(d) also indicates that the nano-inclusion is the ZnSb

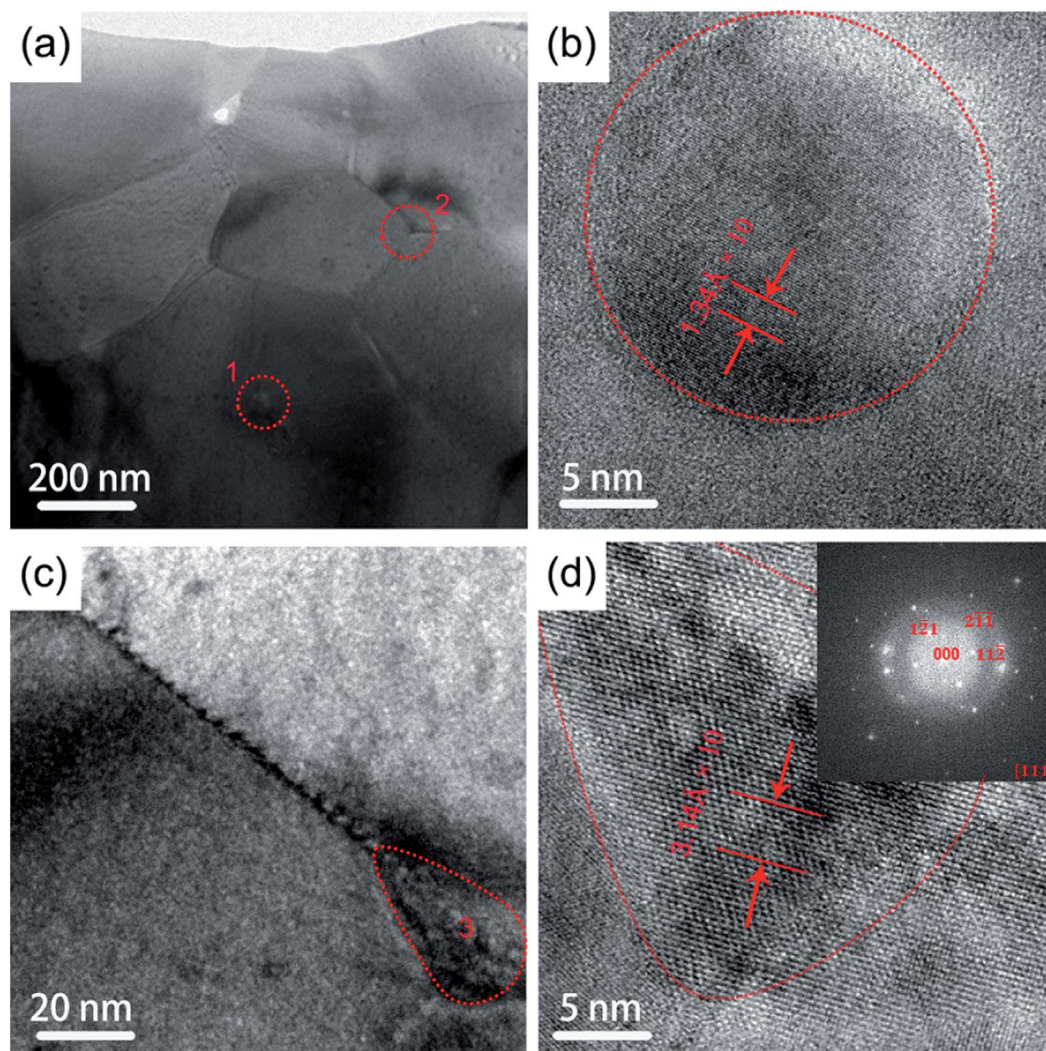


Fig. 4 (a)–(d) Low and high magnification TEM fractographs of the $x = 1.5$ sample. The inset of (d) is the fast Fourier transformation image of (d).

compound. So the context of the $\beta\text{-Zn}_4\text{Sb}_3$ compound in the matrix should be as follows: firstly, it decomposes into Zn and ZnSb nanoparticles during the hot-pressing process, and the ZnSb phase remains as nanoinclusions while Zn particles dissolve and dope into the lattice of $\text{Bi}_{0.4}\text{Sb}_{1.6}\text{Te}_3$ at high temperature during the hot-pressing process; with the temperature cooling down, the solubility of Zn decreases; therefore an undissolved surplus Zn nanoinclusion was also captured in the TEM image.

As shown in Fig. 5(a), the resistivities of the samples with $\beta\text{-Zn}_4\text{Sb}_3$ are lower than that of the $\text{Bi}_{0.4}\text{Sb}_{1.6}\text{Te}_3$ matrix, and it increases with increasing the amount of $\beta\text{-Zn}_4\text{Sb}_3$. As mentioned above, Zn substitution for Bi/Sb increases the hole concentration accordingly. On the other hand, the hole mobility decreases with the increase of the $\beta\text{-Zn}_4\text{Sb}_3$ content. The reduction of carrier mobility is mainly due to two different carrier scattering processes, one is the interface scattering by the nanoinclusions, and the other is the carrier-carrier scattering. With the increase of $\beta\text{-Zn}_4\text{Sb}_3$ content, the amount of nanoinclusions and the hole density increase, therefore the hole mobility decreases rapidly, and the effect of the decrease of the carrier mobility on the electrical resistivity exceeds the increase of carrier concentration. As a result, the electrical

resistivity of the sample with $\beta\text{-Zn}_4\text{Sb}_3$ increases with increasing the amount of $\beta\text{-Zn}_4\text{Sb}_3$.

Fig. 5(b) illustrates the temperature dependence of Seebeck coefficient for the samples. At room temperature, the Seebeck coefficient decreases with the increasing amount of $\beta\text{-Zn}_4\text{Sb}_3$ mainly due to the increase of hole concentration in the sample.⁴ It is noteworthy that the critical temperature corresponding to the peak value of S shifts to higher temperature with increasing the content of $\beta\text{-Zn}_4\text{Sb}_3$, and the peak temperature of the samples with addition of $\beta\text{-Zn}_4\text{Sb}_3$ is around 423 K.

Two possible mechanisms should be attributed to the increased peak temperature of Seebeck coefficients: the major one is due to the increase of hole concentration in the sample which is common in semiconductors. For a given semiconductor, the hole (major) and electron (minor) concentration for a p-type semiconductor should obey the expression¹⁹

$$pn = N_c N_v \exp(-E_g/k_B T) \quad (5)$$

where p and n denote the hole and electron concentration, N_c and N_v are the effective energy state density of the conduction and valence band respectively, E_g is the band gap and k_B is the Boltzmann constant. According to the equation, the increase of hole concentration means the decrease of electron

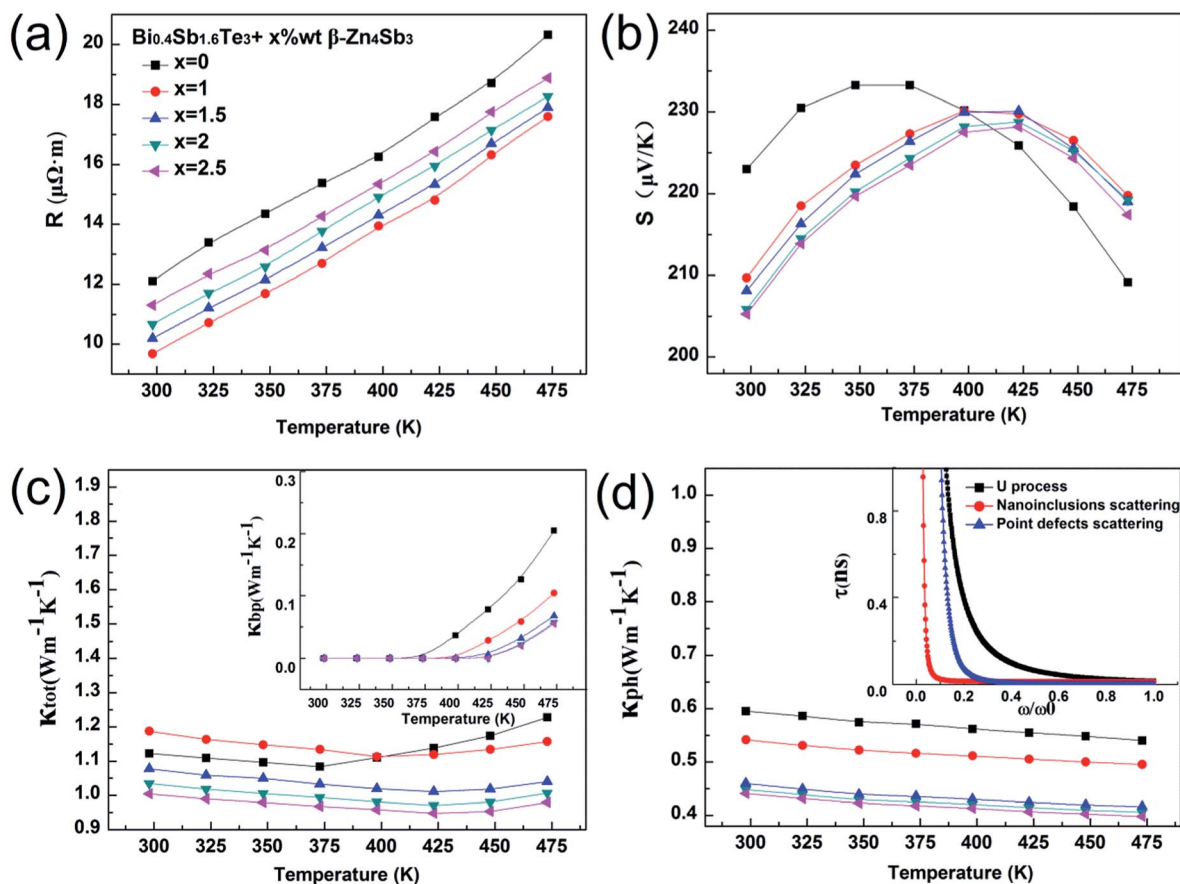


Fig. 5 Thermoelectric properties of the samples with different contents of $\beta\text{-Zn}_4\text{Sb}_3$, (a) electrical resistivity, (b) Seebeck coefficient, (c) total thermal conductivity and bipolar contributions, and (d) calculated phonon thermal conductivities by subtracting the bipolar and electrical thermal conductivities for samples and calculated relaxation times versus reduced frequency of the $x = 1.5$ sample at room temperature.

concentration at a certain temperature. In order to reach the same level of electron concentration or intrinsic excitation, a higher temperature is required. Therefore, the bipolar conduction or intrinsic excitation of the sample with $\beta\text{-Zn}_4\text{Sb}_3$ shifts to higher temperature.

The other mechanism should be ascribed to the interfacial potentials. As supposed by B. Poudel² *et al.*, the interfacial potentials might be formed by the accumulated antisite defects and they scatter more electrons than holes, therefore the motion of electrons (minor carriers) will be inhibited; thus the bipolar transport (intrinsic excitation) occurs at a higher temperature.

Due to the enhanced electrical conductivity and the relatively high Seebeck coefficient at elevated temperature, the calculated power factors of the samples with different amounts of $\beta\text{-Zn}_4\text{Sb}_3$ are also enhanced (see details in ESI. 4, Fig. S3†). Fig. 5(c) shows the temperature dependent thermal conductivities of the sample with different contents of $\beta\text{-Zn}_4\text{Sb}_3$. The $x = 1$ sample has the largest thermal conductivity and the thermal conductivity decreases with the increase of $\beta\text{-Zn}_4\text{Sb}_3$. The thermal conductivity of all samples decreases with the increase of temperature until a critical temperature, which corresponds to the intrinsic excitation of the sample. The critical temperature of thermal conductivity, as shown in the inset of Fig. 5(c), which was derived by the method depicted in ESI. 5, Fig. S4,† presents a similar trend to the Seebeck coefficient.

The phonon thermal conductivities κ_{ph} of all the samples are shown in Fig. 5(d) (see ESI. 5† for details). Obviously, the κ_{ph} of the sample with $\beta\text{-Zn}_4\text{Sb}_3$ is far less than that of the $\beta\text{-Zn}_4\text{Sb}_3$ free sample, and it decreases with increasing the amount of $\beta\text{-Zn}_4\text{Sb}_3$. As is known, κ_{ph} is determined by the phonon scattering process, and low κ_{ph} means more phonon scattering. According to the Matthiessen rule,²⁰ the total relaxation time (τ), which is related to the phonon thermal conductivity by the Callaway model,²¹ is determined by various phonon scattering processes. Considering that the phonon scattering by grain boundaries and carriers can be neglected when the temperature is over 100 K, three main scattering processes that correspond to the point defects, the Umklapp process and the nanoinclusion scattering were taken into account in this case, and their relaxation times were estimated (see ESI. 6† for details) and are shown in the inset of Fig. 5(d).

It can be seen that the point defects and the Umklapp process mostly scatter the medium and high frequency phonons, while the low frequency phonons are mainly scattered by the nanoinclusions. With the introduction of nanoinclusions, a broader spectrum of phonons have been scattered effectively, and therefore the phonon thermal conductivity decreases apparently.

The variation of the ZT values of the samples with temperature is shown in Fig. 6. For comparison, some results from the literature are also depicted in the figure. It is observed that the ZT values of the samples with $\beta\text{-Zn}_4\text{Sb}_3$ have an evident increase and the critical temperature for the maximum ZT shifts to 423 K gradually. The maximum ZT value of 1.44 at 423 K was achieved for the $x = 1.5$ sample. Compared with the best results of single crystals by Yamashita and Tomiyoshi⁵ and polycrystalline ingots

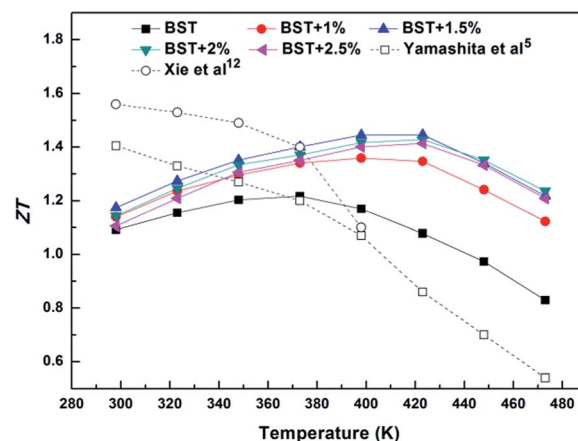


Fig. 6 Variation of the ZT value as a function of temperature for $\text{Bi}_{0.4}\text{Sb}_{1.6}\text{Te}_3 + x \text{ wt}\% \beta\text{-Zn}_4\text{Sb}_3$ and some other results are also listed for comparison.^{5,12}

by Xie *et al.*,¹² the critical temperature for the ZT value in our study increases by about 120 K and the ZT value at 423 K has a 70% improvement. As far as we know, this is the highest ZT value obtained at this temperature.

Conclusions

By means of $\beta\text{-Zn}_4\text{Sb}_3$ addition and decomposition, Zn and ZnSb nanoinclusions were introduced and Zn atoms were doped into the matrix of $\text{Bi}_{0.4}\text{Sb}_{1.6}\text{Te}_3$ successfully. Due to the increased hole concentration by Zn substitution and the band gap broadening by band structure optimization of the ZnSb nanoinclusions, the bipolar conduction of the samples with $\beta\text{-Zn}_4\text{Sb}_3$ addition is suppressed and shifted to higher temperature; on the other hand, the Zn and ZnSb nanoinclusions introduce extra phonon scattering in the matrix and reduce the phonon thermal conductivities of the samples apparently. As a result, the critical temperature corresponding to the maximum ZT value is greatly increased to 423 K, which is about 120 K higher when compared with the conventional Bi_2Te_3 -based materials and a maximum ZT of 1.44 was achieved in the sample with 1.5 wt% $\beta\text{-Zn}_4\text{Sb}_3$ at 423 K. To the best of our knowledge, this is the highest ZT value obtained at such a high temperature for p-type Bi_2Te_3 -based materials. This work is of great importance to expand the application of Bi_2Te_3 -based materials for low grade waste-heat recovery.

Acknowledgements

This work is co-financed by the National Natural Science Foundation of China (Grant no. 51272080), the National Basic Research Program of China (Grant no. 2013CB632500), and the Open Fund of State Key Laboratory of Advanced Technology for Materials Synthesis and Processing, Wuhan University of Technology (no. 2013-KF-3). The technical assistance from the Analytical and Testing Center of HUST is likewise gratefully acknowledged.

Notes and references

- 1 B. C. Sales, *Science*, 2002, **295**, 1248.
- 2 B. Poudel, Q. Hao, Y. Ma, Y. C. Lan, A. Minnich, B. Yu, X. Yan, D. Z. Wang, A. Muto, D. Vashaee, X. Y. Chen, J. M. Liu, M. S. Dresselhaus, G. Chen and Z. F. Ren, *Science*, 2008, **634**, 320.
- 3 Ö. C. Yelgel and G. P. Srivastava, *J. Appl. Phys.*, 2013, **113**, 073709.
- 4 J. P. Heremans, V. Jovovic, E. Toberer, S. Saramat, A. Kurosaki, K. A. Charoenphakdee, S. Yamanaka and G. J. Snyder, *Science*, 2008, **321**, 554.
- 5 O. Yamashita and S. Tomiyoshi, *J. Appl. Phys.*, 2003, **93**, 368.
- 6 L. D. Ivanova, V. Yu, V. Granatkina, N. V. Polikarpova and E. I. Smirnova, *Inorg. Mater.*, 1997, **33**, 558.
- 7 J. Y. Yang, T. Aizawa, A. Yamamoto and T. Ohta, *J. Alloys Compd.*, 2000, **309**, 225.
- 8 X. A. Fan, J. Y. Yang, W. Zhu, S. Q. Bao, X. K. Duan, C. J. Xiao, Q. Q. Zhang and Z. Xie, *J. Phys. D: Appl. Phys.*, 2006, **39**, 5069.
- 9 X. A. Fan, J. Y. Yang, R. G. Chen and W. Zhu, *J. Alloys Compd.*, 2008, **461**, 9.
- 10 D. Li, R. R. Sun and X. Y. Qin, *Intermetallics*, 2011, **19**, 2002.
- 11 J. J. Shen, T. J. Zhu, X. B. Zhao, S. N. Zhang, S. H. Yang and Z. Z. Yin, *Energy Environ. Sci.*, 2010, **3**, 1519.
- 12 W. J. Xie, X. F. Tang, Y. Yan, Q. Zhang and T. M. Tritt, *Appl. Phys. Lett.*, 2009, **94**, 102111.
- 13 Q. H. Jiang, H. X. Yan, J. Khaliq, H. P. Ning, S. Grasso, K. Simpsonb and M. J. Reece, *J. Mater. Chem. A*, 2014, **2**, 5785.
- 14 C. W. Chan, J. L. Chin and A. P. Roskily, *Appl. Therm. Eng.*, 2013, **50**, 1257.
- 15 T. Caillat, J. P. Fleurial and A. Borshchevsky, *J. Phys. Chem. Solids*, 1997, **58**, 1119.
- 16 J. Y. Yang and R. G. Chen, *J. Alloys Compd.*, 2006, **407**, 330.
- 17 T. Huang, J. Jiang, Y. K. Xiao, Y. B. Zhai, S. H. Yang and G. J. Xu, *J. Mater. Chem. A*, 2013, **1**, 966.
- 18 Z. Hou, Z. Zhu, M. Huang and Y. Yang, *PhysChemComm*, 2003, **6**, 47.
- 19 W. S. Liu, B. P. Zhang, J. F. Li, H. L. Zhang and L. D. Zhao, *J. Appl. Phys.*, 2007, **102**, 103717.
- 20 X. H. Yang and X. Y. Qin, *Appl. Phys. Lett.*, 2010, **97**, 192101.
- 21 J. Callaway and H. C. Vonbaeyer, *Phys. Rev.*, 1960, **120**, 1149.